nature materials

Article

https://doi.org/10.1038/s41563-023-01713-y

Dynamically tunable moiré exciton Rydberg states in a monolayer semiconductor on twisted bilayer graphene

Received: 15 March 2023

Accepted: 2 October 2023

Published online: 4 January 2024

Check for updates

Minhao He[1,10], Jiaqi Cai[1,10], Huiyuan Zheng[2,10], Eric Seewald[3], Takashi Taniguchi[4], Kenji Watanabe[5], Jiaqiang Yan[6,7], Matthew Yankowitz[1,8], Abhay Pasupathy[3], Wang Yao[2,9] ✉ & Xiaodong Xu[1,8] ✉

Moiré excitons are emergent optical excitations in two-dimensional semiconductors with moiré superlattice potentials. Although these excitations have been observed on several platforms, a system with dynamically tunable moiré potential to tailor their properties is yet to be realized. Here we present a continuously tunable moiré potential in monolayer WSe_2, enabled by its proximity to twisted bilayer graphene (TBG) near the magic angle. By tuning local charge density via gating, TBG provides a spatially varying and dynamically tunable dielectric superlattice for modulation of monolayer WSe_2 exciton wave functions. We observed emergent moiré exciton Rydberg branches with increased energy splitting following doping of TBG due to exciton wave function hybridization between bright and dark Rydberg states. In addition, emergent Rydberg states can probe strongly correlated states in TBG at the magic angle. Our study provides a new platform for engineering moiré excitons and optical accessibility to electronic states with small correlation gaps in TBG.

The ability to engineer and control the wave function of quasi-particles is of critical importance in quantum science and technologies. The recent creation of synthetic moiré quantum matter, formed by stacking layered van der Waals materials, provides a new and powerful means to achieve such control[1–3]. One example is the moiré excitons found in transition metal dichalcogenide (TMD) moiré superlattices[4–8], which act as novel optical excitations residing in a smoothly varying periodical moiré potential. Compared with free two-dimensional excitons, the introduction of moiré potential can markedly modify properties with effects including new optical resonance due to zone folding[6,9], optical selection rules determined by local sublattice symmetry[5,7] and quantum optical effects from deep potential confinement[10,11]. In addition to single-trap physics, the periodic superlattice potential enables collective effects such as topological excitons[12], excitonic insulators[13], exciton-correlated electron bound state[14] and dipolar exciton solids[15,16].

Since the moiré potential and its lattice geometry play a critical role in the physical properties of moiré excitons, it is desirable to achieve dynamic tunability and even an on/off switch with which to control moiré potential. Although spatial periodicity can be engineered by lattice mismatch and/or twist angle during sample

[1]Department of Physics, University of Washington, Seattle, WA, USA. [2]Department of Physics, University of Hong Kong, Hong Kong, China. [3]Department of Physics, Columbia University, New York, NY, USA. [4]International Center for Materials Nanoarchitectonics, National Institute for Materials Science, Tsukuba, Japan. [5]Research Center for Functional Materials, National Institute for Materials Science, Tsukuba, Japan. [6]Materials Science and Technology Division, Oak Ridge National Laboratory, Oak Ridge, TN, USA. [7]Department of Materials Science and Engineering, University of Tennessee, Knoxville, TN, USA. [8]Department of Materials Science and Engineering, University of Washington, Seattle, WA, USA. [9]HKU-UCAS Joint Institute of Theoretical and Computational Physics at Hong Kong, Hong Kong, China. [10]These authors contributed equally: Minhao He, Jiaqi Cai, Huiyuan Zheng. ✉e-mail: wangyao@hku.hk; xuxd@uw.edu

https://doi.org/10.1038/s41563-023-01713-y

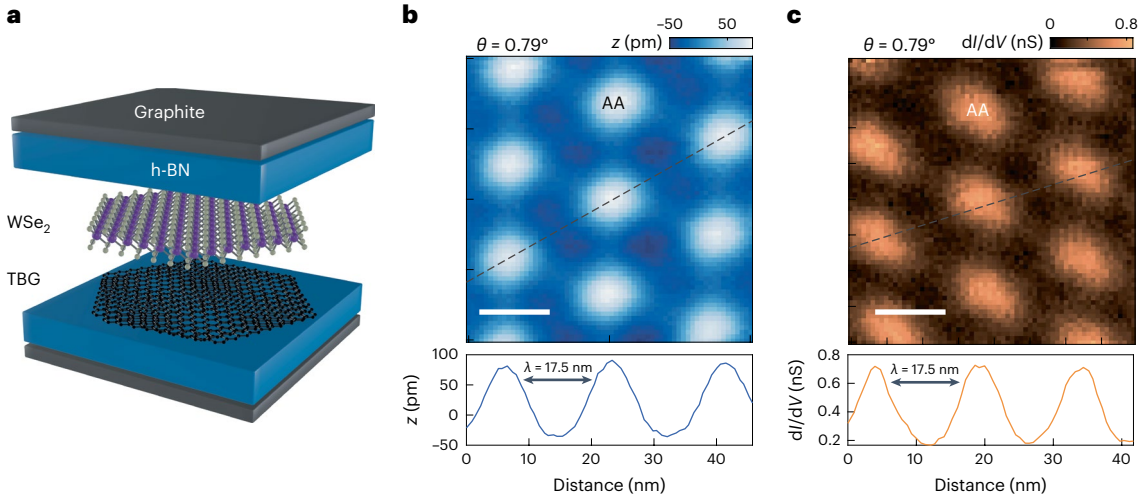

Fig. 1 | Localized charge distribution in TBG and its periodic screening of adjacent WSe_2. a, Schematic of the device structure in which a monolayer WSe_2 is stacked on top of the TBG; the heterostructure is then further encapsulated with h-BN on both sides with top and bottom graphite gates. **b**, Top, STM topography image of a $\theta = 0.79°$ TBG sample. Scale bar, 10 nm. Bottom, linecut of the topography image along the dashed line. **c**, Differential conductance d*I*/d*V*, i.e. LDOS, at charge neutrality in the valence flat band on the same TBG sample. Spectroscopic measurements were performed with junction normalization of $V = 0.5$ V and $I = 100$ pA. Under these conditions the STM tip followed the topographic height of the sample well, with contrast arising from spectroscopic variation. Scale bar, 10 nm.

fabrication, achieving wide-range, continuous tunability of moiré potential depth remains challenging owing to the intertwined electronic and structural origin of moiré potential[17,18]. An alternative solution is direct engineering of the dielectric environment of monolayer TMDs. The Wannier–Mott nature of excitons in monolayer TMDs makes them extremely sensitive to their dielectric environment[19,20], especially so for exciton Rydberg states with large Bohr radius[19,21,22]. This effect has been successfully utilized to engineer exciton binding energy by substrate design[20,23]. As a result, excitonic moiré potential arising from the periodic modulation of both quasi-particle band gap and exciton binding energy can be engineered in monolayer TMDs placed directly onto a dielectric superlattice. Recent work has demonstrated the periodic dielectric screening effect in a heterostructure of monolayer WSe_2 and a moiré superlattice of graphene on hexagonal boron nitride (h-BN)[24], where the presence of moiré potential is revealed by high-energy Umklapp states of the 2s exciton. Moreover, periodic dielectric screening of electron-hole Coulomb exchange can also be explored for engineering of spatial valley textures to enable novel excitonic functionalities[25].

Here we employ twisted bilayer graphene (TBG) as a functional substrate to engineer a dynamically tunable moiré potential in monolayer TMDs. We show that this platform enables the control of excitonic orbitals, and thus a tunable hybridization between bright and dark exciton Rydberg states, manifested as brightened exciton states versus doping. Figure 1a depicts the device structure. For TBG near the magic angle, flat electronic bands enable the generation of a spatially modulated dielectric constant with its strength proportional to the localized but tunable charge density. Taking a TBG sample with a twist angle of 0.79° as an example, scanning tunnelling microscopy (STM) imaging shows local atomic registry varying between AA sites (carbon atoms in the two layers overlap vertically) and AB/BA sites (Bernal stacking) within a single moiré unit cell[26–28] (Fig. 1b). Charge distribution is highly localized on AA sites and forms a triangular lattice, as illustrated on a map of local density of states (LDOS; Fig. 1c). Gating of TBG enables direct control of charge density at AA sites while always maintaining the same overall spatial pattern. Interfacing TBG with monolayer TMD could thus realize a dynamically tunable and spatially periodic dielectric environment for monolayer excitons.

Observation of moiré exciton Rydberg states

We studied a total of four WSe_2/TBG devices here, in which the twist angle of TBG ranged from close to 0° (that is, almost complete relaxation to Bernal stacking) to the magic angle (~1.1°) (Supplementary Fig. 1). The devices were constructed with dual-gated Hall bar geometry, allowing for individual control over displacement field D and carrier density n (Fig. 1a; see Methods for details). Electrical transport measurements were first performed to characterize each device and determine TBG twist angle, θ (Supplementary Figs. 2–4). Specifically we measured the Hall coefficient (R_H) and Landau fan diagram to determine carrier density corresponding to the full filling of the lowest flat bands (Methods). We then used optical reflection spectroscopy to study excitons in monolayer WSe_2. All optical spectroscopy data were acquired at a nominal temperature of 5 K unless otherwise specified.

In Fig. 2a we show the gate-dependent optical reflectance contrast ($\Delta R/R$) of a reference sample, where monolayer WSe_2 is adjacent to TBG with a relaxed twist angle (see Supplementary Fig. 2 for transport measurements). Compared with the reflectance contrast of isolated monolayer WSe_2 (Supplementary Fig. 5)[29–31], gate-dependent $\Delta R/R$ of the WSe_2/TBG heterostructure is dominated by the 1s exciton at 1.72 eV with negligible energy shift as a function of doping. This is consistent with the band alignment of graphene and WSe_2: Fermi energy can be gate-tuned within the TBG flat band but always remains deep within the WSe_2 band gap[24] (Fig. 2c, inset).

In addition, a 2s exciton was observed at ~80 meV above the 1s exciton at zero doping. Exciton 1s–2s splitting, which implicitly connects to exciton binding energy, is much smaller than the 130 meV splitting observed in monolayer WSe_2 encapsulated by h-BN (Supplementary Fig. 5). The reduction in exciton binding energy and suppression of oscillator strength of the 2s exciton[20] indicate a strong dielectric screening effect arising from TBG[20]. The dielectric screening effect is enhanced as charge carriers are electrostatically doped into the TBG, as indicated by the continuous suppression of the oscillator strength of the 2s exciton and red-shift of its peak energy.

We next show optical reflection measurements of a monolayer WSe_2 on TBG with twist angle $\theta = 0.8°$ (Fig. 2c), with θ determined from the transport measurements of R_H (Fig. 2d). The tunable moiré dielectric screening effect was revealed by the emergence of exciton

https://doi.org/10.1038/s41563-023-01713-y

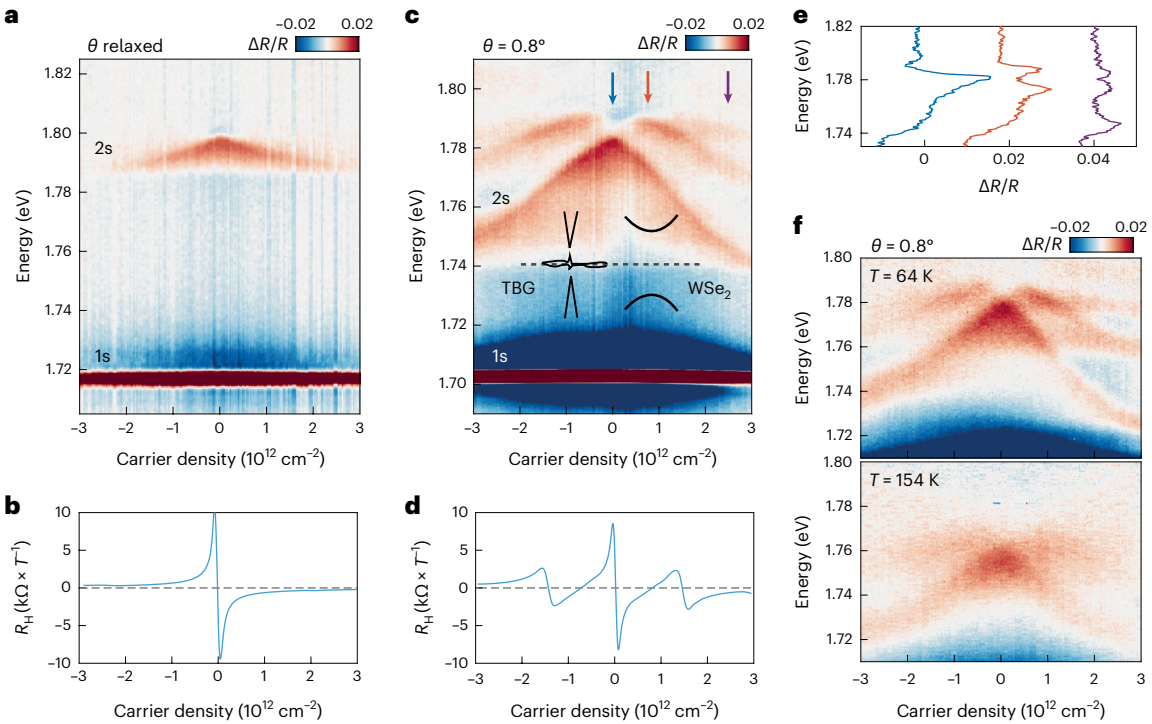

Fig. 2 | Moiré exciton Rydberg states in monolayer WSe_2 on TBG. **a**,**c**, Reflectance contrast ($\Delta R/R$) as a function of the carrier density of monolayer WSe_2 on TBG with twist angle θ relaxed (**a**) and twist angle $\theta = 0.8°$ (**c**). Band alignment of monolayer WSe_2 and TBG is shown in inset in **c**. Data were recorded at 5 K. **b**,**d**, R_H of TBG in the device as shown in **a** (**b**) and **c** (**d**). **e**, Linecuts of $\Delta R/R$ in the device with TBG $\theta = 0.8°$, at carrier density labelled by arrows in **c**, with $n = 0$, $0.73 \times 1{,}012$ and $2.43 \times 1{,}012$ cm^{-2} for blue, orange and purple lines, respectively. **f**, $\Delta R/R$ of the same device with TBG $\theta = 0.8°$ measured at $T = 64$ K and $T = 154$ K.

Rydberg states following gating. As seen in Fig. 2c, the 2s exciton peak is the only exciton Rydberg state observed at charge neutrality, consistent with that of the reference sample. A strong excitonic peak emerged at slightly higher energy following doping of TBG to $n \approx \pm 0.5 \times 10^{12}$ cm^{-2}, and dispersed to lower energy with further doping. This was followed by the emergence of a second, weaker excitonic peak at $n \approx 1.5 \times 10^{12}$ cm^{-2} on the electron-doped side that dispersed only weakly with TBG doping (Supplementary Fig. 6). Energy splitting between exciton Rydberg states also increased with doping, highlighted by spectral linecuts taken at selected dopings (Fig. 2e). These emergent peaks were reproducible across the whole sample and were robust up to ~150 K (Fig. 2f). Similar phenomena were also observed in another device with TBG $\theta = 0.93°$ (Supplementary Fig. 7).

Figure 3a shows the extracted relative energy, ΔE, of Rydberg states with respect to their corresponding 1s states, measured in WSe_2/TBG devices with varying twist angle. At zero doping a single 2s state was observed 80 meV above the 1s state, independent of TBG twist angle. This reveals the weak moiré modulation of the dielectric screening when TBG was held at charge neutrality, consistent with the expectation of uniform underlying charge distribution in neutral TBG. In contrast, devices with a well-defined TBG moiré superlattice rapidly developed a strong moiré potential with doping as a result of the periodically modulated charge distribution in TBG (Fig. 1c). Whereas small-angle TBG with near-Bernal stacking exhibited only a 2s exciton, our observation of multiple gate-tunable excitons in samples with higher twist angle is consistent with the formation of moiré exciton Rydberg states. This clearly demonstrates the importance of modulation from the unique charge distribution in TBG.

Hybridization of excitons with distinct orbitals

We now turn to determining the origin of these new Rydberg states (Supplementary Note 1). Excitonic zone-folding effects due to the moiré superlattice provide one possible explanation, as explored in previous works[6,9,24]. In brief, the periodic potential folds the original exciton dispersion into a moiré mini-Brillouin zone. When the folded bands are within a light cone of finite optical oscillator strength, new excitons in the form of Umklapp states arise at higher energy. To examine this potential explanation we extracted the energy difference between the two lowest Rydberg states. Figure 3b shows that this difference from various twist angles almost collapsed into a single curve as a function of doping, because the energy separation of an Umklapp state with respect to ground state is proportional to θ^2 and is independent of doping. Our observation of an energy separation that is almost independent of θ but highly tunable with TBG doping does not support such a possibility[24]. We also discuss other, less likely, exotic possibilities involving a strongly interacting interlayer exciton - Fermi sea (Supplementary Note 3).

In fact, the moiré potential effect in this zone-folding picture affects only exciton centre-of-mass motion, assuming that the Rydberg orbitals of relative electron-hole motion remain intact[32–34]. This assumption breaks down once the Bohr radius of Rydberg states[35,36] becomes comparable to the length scale of rapid dielectric variation[37]. Microscopically, the steep charge distribution in TBG (Fig. 1b) adds additional terms to the original Hamiltonian of the exciton in monolayer TMDs, which can be understood as a scattering potential that affects both centre-of-mass and electron-hole relative motion (Supplementary Note 1). Effectively this can introduce off-diagonal coupling between the otherwise orthogonal Rydberg states with Bohr radii comparable to, or larger than, the length scale of TBG charge distribution. Therefore, hybridization between excitonic Rydberg states that are close in terms of energy becomes appreciable. Moreover, through such hybridization, dark Rydberg states can acquire finite oscillator strength from a hybridized component of bright ones. As a result, the exciton hybridization effect driven by the enhanced moiré potential of the doped TBG can generate new, bright excitonic features in the optical spectrum as the corresponding dark states acquire oscillator strength.

https://doi.org/10.1038/s41563-023-01713-y

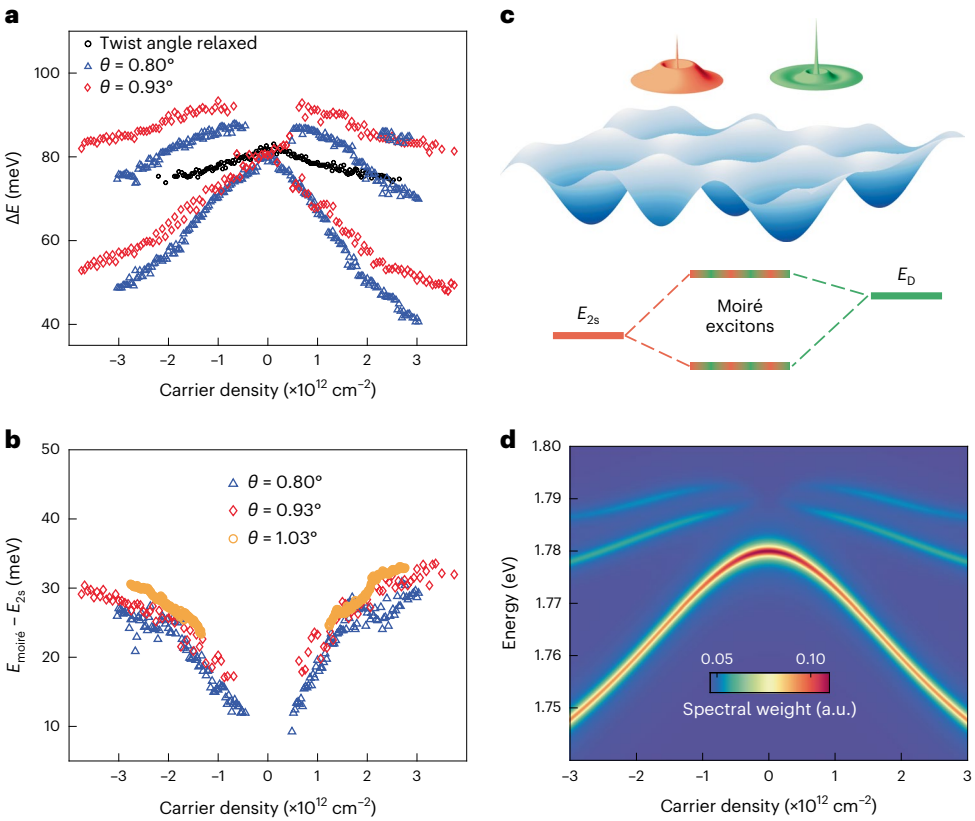

Fig. 3 | Tunable hybridization of exciton Rydberg states. a, Relative energy (ΔE) of exciton Rydberg states with respect to 1s exciton in WSe_2/TBG at varying twist angle, θ: $\Delta E = E - E_{1s}$; E and E_{1s} are exciton Rydberg state and 1s exciton energy, respectively. **b**, Energy difference between higher-energy moiré excitons and the 2s exciton, plotted as a function of TBG doping in samples with varying θ. **c**, Top, schematic of the 2s exciton and another dark or dim exciton (3s Rydberg state in the model) situated in a rapidly varying moiré potential and with periodicity comparable to the Bohr radius of the excitons themselves. Bottom, the exciton hybridization effect that results in moiré excitons inheriting the spectral weight of the original 2s exciton state. **d**, Simulated spectral weight of hybridized exciton Rydberg states brightened by moiré potential. Calculation details can be found in Supplementary Note 2. a.u., Arbitrary units.

We now present a phenomenological model to describe the exciton hybridization effect with doping (Methods). We consider that a moiré potential couples the 2s state to a nearby optically dark or dim state (that is, 3s and 4s Rydberg states[35]) with coupling strength t that grows with doping (Fig. 3c). Figure 3d shows a calculation of the spectrum of excitonic states (oscillator strength) as a function of TBG doping, reproducing the main features of our experiment. The calculation shows that moiré-hybridized excitonic states brighten as moiré potential is enhanced. Moreover, splitting of these hybridized states with the 2s exciton also increases, reflecting increased coupling strength.

Optical sensing of strongly correlated states in magic-angle TBG

The highly localized charge density in TBG is fundamental in realizing the gate-tunable periodic potential in its adjacent monolayer semiconductor. While this statement holds true for a large range of TBG twist angles, of particular interest is a narrower range near the magic angle of 1.1°, at which interlayer hopping interference creates extremely flat low-energy electronic bands[38]. The kinetic energy of electrons is suppressed within these flat bands and the system becomes dominated by strong Coulomb interactions. A rich phase diagram of strongly correlated states has been reported in magic-angle TBG[39–44], including correlated insulators, superconductors, orbital magnetism and the quantum anomalous Hall effect.

Figure 4a shows the $\Delta R/R$ of moiré exciton Rydberg states of a monolayer WSe_2 adjacent to magic-angle TBG with $\theta = 1.03°$, measured at $T = 2$ K. Unlike the continuous energy red-shift demonstrated in Fig. 2, the 2s exciton follows a sawtooth pattern in which its energy temporarily blue-shifts near certain charge densities but exhibits an overall red-shift trend as TBG is doped (Supplementary Fig. 8). Blue-shifts of the 2s exciton are accompanied by enhancement in its oscillator strength which, combined, indicates reduced dielectric screening at these specific carrier densities. To help understand this exciton spectrum we conducted electrical transport measurements with the device shown in the top panel of Fig. 4b (further transport characterization is shown in Supplementary Fig. 4). We highlight the high quality of our sample by the superconductivity state emergent below $T = 1$ K at $\upsilon = -2 - \delta$, as seen in the inset. Within the flat bands between $\nu = \pm 4$, WSe_2/TBG is characterized by a cascade of strongly correlated states, either insulating or weakly resistive, at almost all values of integer filling factor $\nu = -3, -2, 0, 1, 2$ and 3, consistent with previous reports[45–47]. A variety of symmetry-broken states have been proposed as ground-state candidates in magic-angle TBG[48], which was further complicated by induced spin-orbit coupling from the proximate WSe_2 (refs. 45–47) in our device. The exact nature of these correlated states remains an open question, and is currently under investigation.

We observed a clear connection between sample resistance (R_{xx}) and 2s–1s splitting ΔE (Fig. 4b). We identified a one-to-one correspondence for the maxima of energy blue-shifts and oscillator strength of the 2s exciton with the correlated insulators at $\upsilon = +1, +2$ and $+3$ seen in transport. The correlated insulating state in hole-doped states is not as clear as that in the electron-doped side. In the static limit, Thomas–Fermi screening established a direct relationship between dielectric constant (ε) and electronic compressibility, $\partial n/\partial \mu$. As a result, the peak of 2s exciton spectrum can serve as an optical sensor of local

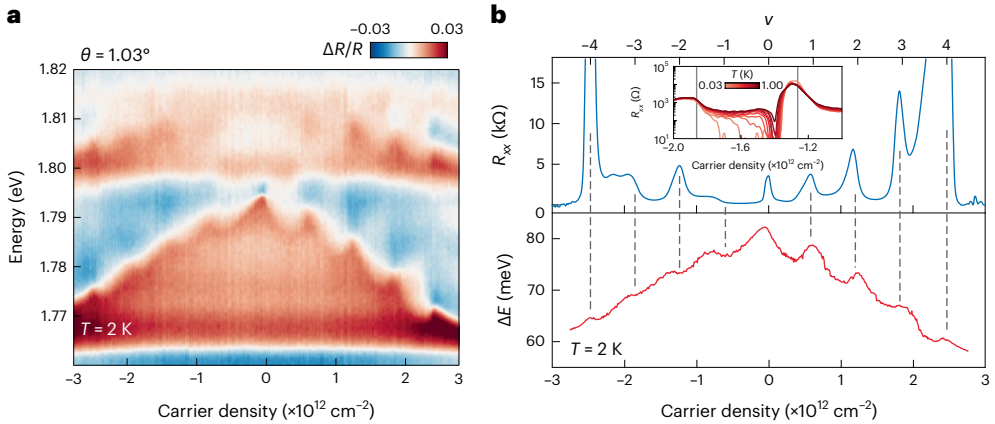

Fig. 4 | Exciton Rydberg state sensing of strongly correlated states in magic-angle TBG. a, Reflectance contrast ($\Delta R/R$) of a monolayer WSe_2 located on top of magic-angle TBG with $\theta = 1.03°$. Data were taken at $T = 2$ K. **b**, Top, resistance (R_{xx}) of TBG at $T = 2$ K. Bottom, relative energy (ΔE) of the 2s exciton ($\Delta E = E_{2s} - E_{1s}$), extracted from **a** (bottom), as a function of carrier density. Inset shows the temperature dependence of TBG R_{xx} in the vicinity of filling factor $\nu = -2$ with emergent superconductivity at temperature below $T = 1$ K, demonstrating the high quality of the sample.

compressibility. We note that further theoretical work is needed to establish a quantitative relation bridging the exciton spectrum with the dielectric superlattice, as well as electronic compressibility.

Conclusions

In conclusion, our work develops a continuously tunable moiré potential for monolayer semiconductors, arising due to pronounced dielectric screening from the unique charge distribution in TBG. This creates opportunities for engineering of trapping arrays for monolayer excitons with selectivity to their specific Rydberg orbitals, and to tailoring of exciton dynamics and many-body interactions using this periodic potential landscape. Exciton Rydberg states can also be exploited as a dynamical sensor to enrich the toolbox for probing the equilibrium states and dynamics of correlated phenomena of interest in magic-angle TBG, such as charge order, magnetic order and superconductivity.

Online content

Any methods, additional references, Nature Portfolio reporting summaries, source data, extended data, supplementary information, acknowledgements, peer review information; details of author contributions and competing interests; and statements of data and code availability are available at https://doi.org/10.1038/s41563-023-01713-y.

References

1. Andrei, E. Y. et al. The marvels of moiré materials. *Nat. Rev. Mater.* **6**, 201–206 (2021).
2. Kennes, D. M. et al. Moiré heterostructures as a condensed-matter quantum simulator. *Nat. Phys.* **17**, 155–163 (2021).
3. Mak, K. F. & Shan, J. Semiconductor moiré materials. *Nat. Nanotechnol.* **17**, 686–695 (2022).
4. Yu, H., Liu, G.-B., Tang, J., Xu, X. & Yao, W. Moiré excitons: from programmable quantum emitter arrays to spin-orbit–coupled artificial lattices. *Sci. Adv.* **3**, e1701696 (2017).
5. Seyler, K. L. et al. Signatures of moiré-trapped valley excitons in $MoSe_2/WSe_2$ heterobilayers. *Nature* **567**, 66–70 (2019).
6. Jin, C. et al. Observation of moiré excitons in WSe_2/WS_2 heterostructure superlattices. *Nature* **567**, 76–80 (2019).
7. Tran, K. et al. Evidence for moiré excitons in van der Waals heterostructures. *Nature* **567**, 71–75 (2019).
8. Huang, D., Choi, J., Shih, C.-K. & Li, X. Excitons in semiconductor moiré superlattices. *Nat. Nanotechnol.* **17**, 227–238 (2022).
9. Naik, M. H. et al. Intralayer charge-transfer moiré excitons in van der Waals superlattices. *Nature* **609**, 52–57 (2022).
10. Zhang, L. et al. Van der Waals heterostructure polaritons with moiré-induced nonlinearity. *Nature* **591**, 61–65 (2021).
11. Baek, H. et al. Highly energy-tunable quantum light from moiré-trapped excitons. *Sci. Adv.* **6**, eaba8526 (2020).
12. Wu, F., Lovorn, T. & MacDonald, A. H. Topological exciton bands in moiré heterojunctions. *Phys. Rev. Lett.* **118**, 147401 (2017).
13. Chen, D. et al. Excitonic insulator in a heterojunction moiré superlattice. *Nat. Phys.* **18**, 1171–1176 (2022).
14. Tang, Y. et al. Simulation of Hubbard model physics in WSe_2/WS_2 moiré superlattices. *Nature* **579**, 353–358 (2020).
15. Gu, J. et al. Dipolar excitonic insulator in a moiré lattice. *Nat. Phys.* **18**, 395–400 (2022).
16. Zhang, Z. et al. Correlated interlayer exciton insulator in heterostructures of monolayer WSe_2 and moiré WS_2/WSe_2. *Nat. Phys.* **18**, 1214–1220 (2022).
17. Shabani, S. et al. Deep moiré potentials in twisted transition metal dichalcogenide bilayers. *Nat. Phys.* **17**, 720–725 (2021).
18. Li, H. et al. Imaging moiré flat bands in three-dimensional reconstructed WSe_2/WS_2 superlattices. *Nat. Mater.* **20**, 945–950 (2021).
19. Chernikov, A. et al. Exciton binding energy and nonhydrogenic Rydberg series in monolayer WS_2. *Phys. Rev. Lett.* **113**, 076802 (2014).
20. Raja, A. et al. Coulomb engineering of the bandgap and excitons in two-dimensional materials. *Nat. Commun.* **8**, 15251 (2017).
21. He, K. et al. Tightly bound excitons in monolayer WSe_2. *Phys. Rev. Lett.* **113**, 026803 (2014).
22. Wang, G. et al. Giant enhancement of the optical second-harmonic emission of WSe_2 monolayers by laser excitation at exciton resonances. *Phys. Rev. Lett.* **114**, 097403 (2015).
23. Utama, M. I. B. et al. A dielectric-defined lateral heterojunction in a monolayer semiconductor. *Nat. Electron.* **2**, 60–65 (2019).
24. Xu, Y. et al. Creation of moiré bands in a monolayer semiconductor by spatially periodic dielectric screening. *Nat. Mater.* **20**, 645–649 (2021).
25. Yang, X.-C., Yu, H. & Yao, W. Chiral excitonics in monolayer semiconductors on patterned dielectrics. *Phys. Rev. Lett.* **128**, 217402 (2022).
26. Xie, Y. et al. Spectroscopic signatures of many-body correlations in magic-angle twisted bilayer graphene. *Nature* **572**, 101–105 (2019).
27. Kerelsky, A. et al. Maximized electron interactions at the magic angle in twisted bilayer graphene. *Nature* **572**, 95–100 (2019).

28. Choi, Y. et al. Electronic correlations in twisted bilayer graphene near the magic angle. *Nat. Phys.* **15**, 1174–1180 (2019).
29. Jones, A. M. et al. Optical generation of excitonic valley coherence in monolayer WSe_2. *Nat. Nanotechnol.* **8**, 634–638 (2013).
30. Mak, K. F. et al. Tightly bound trions in monolayer MoS_2. *Nat. Mater.* **12**, 207–211 (2013).
31. Wagner, K. et al. Autoionization and dressing of excited excitons by free carriers in monolayer WSe_2. *Phys. Rev. Lett.* **125**, 267401 (2020).
32. Lamouche, G. & Lépine, Y. Ground-state energy of an exciton in a quantum-dot superlattice grown on a terraced substrate. *Phys. Rev. B* **54**, 4811–4819 (1996).
33. Tkach, N. V., Makhanets, A. M. & Zegryae, G. G. Electrons, holes, and excitons in a superlattice composed of cylindrical quantum dots with extremely weak coupling between quasiparticles in neighboring layers of quantum dots. *Semiconductors* **36**, 511–518 (2002).
34. Suris, R. A. Wannier–Mott excitons in semiconductors with a superlattice. *Semiconductors* **49**, 807–813 (2015).
35. Stier, A. V. et al. Magnetooptics of exciton Rydberg states in a monolayer semiconductor. *Phys. Rev. Lett.* **120**, 057405 (2018).
36. Goryca, M. et al. Revealing exciton masses and dielectric properties of monolayer semiconductors with high magnetic fields. *Nat. Commun.* **10**, 4172 (2019).
37. Semina, M. A. & Suris, R. A. Localized excitons and trions in semiconductor nanosystems. *Phys. Uspekhi* **65**, 111–130 (2022).
38. Bistritzer, R. & MacDonald, A. H. Moiré bands in twisted double-layer graphene. *Proc. Natl Acad. Sci. USA* **108**, 12233–12237 (2011).
39. Cao, Y. et al. Correlated insulator behaviour at half-filling in magic-angle graphene superlattices. *Nature* **556**, 80–84 (2018).
40. Cao, Y. et al. Unconventional superconductivity in magic-angle graphene superlattices. *Nature* **556**, 43–50 (2018).
41. Yankowitz, M. et al. Tuning superconductivity in twisted bilayer graphene. *Science* **363**, eaav1910 (2019).
42. Lu, X. et al. Superconductors, orbital magnets and correlated states in magic-angle bilayer graphene. *Nature* **574**, 653–657 (2019).
43. Sharpe, A. L. et al. Emergent ferromagnetism near three-quarters filling in twisted bilayer graphene. *Science* **365**, 605–608 (2019).
44. Serlin, M. et al. Intrinsic quantized anomalous Hall effect in a moiré heterostructure. *Science* **367**, 900–903 (2020).
45. Arora, H. S. et al. Superconductivity in metallic twisted bilayer graphene stabilized by WSe_2. *Nature* **583**, 379–384 (2020).
46. Lin, J.-X. et al. Spin-orbit–driven ferromagnetism at half moiré filling in magic-angle twisted bilayer graphene. *Science* **375**, 437–441 (2022).
47. Polski, R. et al. Hierarchy of symmetry breaking correlated phases in twisted bilayer graphene. Preprint at *arXiv* https://doi.org/10.48550/arxiv.2205.05225 (2022).
48. Lian, B. et al. Twisted bilayer graphene. IV. Exact insulator ground states and phase diagram. *Phys. Rev. B* **103**, 205414 (2021).

Methods

Sample fabrication

Heterostructures of graphite/h-BN/WSe_2/TBG/h-BN/graphite were assembled using a standard dry-transfer technique with a polycarbonate/polydimethylsiloxane stamp, and transferred onto a Si/SiO_2 wafer. The TBG stack was fabricated using the tear-and-stack method. We used 3–5-nm graphite as the bottom gate whereas three-to-five-layer graphene was used for the top gate, to minimize its optical absorption. We exerted no intentional control over the twist angle between WSe_2 and its adjacent graphene layer during the stacking process. CHF_3/O_2 and O_2 plasma etching, followed by electron beam lithography, were used to define Hall bar geometry and Cr/Au contacts were added finally using electron beam evaporation.

Transport measurements

Transport measurements were conducted in a Quantum Design physical property measurement system. Measurements were performed with a 1–5 nA alternating excitation current at either 13.3 or 13.7 Hz. Current and voltage were preamplified by DL 1211 (DL instruments) and SR560 (Stanford Research Systems), respectively and then read out by SR830/SR860 lock-in amplifiers (Stanford Research Systems). Gate voltages were supplied by either a NI DAQ (National Instruments) or Keithley 2450 (Tektronix). A global Si gate was sometimes used to reduce contact resistance issues.

Dual-gate device geometry enables independent control of both D and n. The relationship between top and bottom gate voltages (V_t, V_b) and n and D are given by $n = (V_tC_t + V_bC_b)/e$ and $D = (V_tC_t - V_bC_b)/2\epsilon_0$, where C_t and C_b are the top and bottom gate capacitances per unit area, respectively, and ϵ_0 is vacuum permittivity.

Filling factor ν is defined as the number of electrons per moiré unit cell. Full filling of eightfold-degenerate flat bands in TBG corresponds to four electrons (holes) per moiré unit cell, $\nu = \pm 4$. Carrier densities corresponding to full fillings $\nu = \pm 4$ can be determined by measuring R_H at a small magnetic field, B: $R_H = (\rho_{xy}(B) - \rho_{xy}(-B))/(2B)$. Hall carrier density ($n_H = 1/eR_H$) and reverse carrier type (from electron to hole, or vice versa) across full fillings $\nu = \pm 4$ can be identified as the zero crossing in R_H measurements. Twist angle is then determined following the relationship $n = 8\theta^2/\sqrt{3}a^2$, where $a = 0.246$ nm is the graphene lattice constant. For magic-angle TBG this was further confirmed by fitting the observed quantum Hall states and Chern insulators with the allowed Hofstadter states in the Wannier diagram. Twist angle determination from transport can then be compared with exciton Rydberg state energy blue-shift observed by reflectance contrast spectroscopy. For TBG with smaller twist angle we did not observe exciton Rydberg state energy blue-shift corresponding to full filling of the lowest flat bands at $\nu = \pm 4$, indicating the metallic nature of $\nu = \pm 4$ states at this twist angle[45].

Reflectance contrast spectroscopy

Optical reflection measurements were performed using a home-built confocal microscope. Samples were mounted either on the cold head of a close-cycled Montana cryostat, with temperature maintained at 5 K, or inside a He-exchange, gas-cooled cryostat (Quantum Design OptiCool), with temperature maintained at 2 K. A halogen lamp (Thorlabs, SLS201L) was used as a white light source. The output of the white light was coupled to a single-mode fibre and then collimated with a triplet collimator. The beam was then focused to a waist of ~1 μm on the sample by a ×40 objective lens (numerical aperture 0.6). The excitation power of the white light was kept <10 nW. Reflection signals were collected and directed into a spectrometer, where they were dispersed by a diffraction grating and detected on a silicon charge-coupled device (Princeton PyLoN).

Reflectance contrast ($\Delta R/R$) is defined as $\Delta R/R = (R - R_0)/R_0$, where R denotes the reflection spectrum on the sample and R_0 the background reflection spectrum. For $\Delta R/R$ measurements on monolayer WSe_2 (Supplementary Fig. 5), the background reflection spectrum was taken at an adjacent spot without WSe_2. For $\Delta R/R$ measurements on the WSe_2/TBG heterostructure, the signal from Rydberg states was much weaker and hence the background reflection spectrum for those measurements was taken at the same spot on the sample but with sample gate-tuned to a high doping level. To minimize overtime drift of the $\Delta R/R$ background, the R_0 spectrum was recorded periodically[49] (approximately every 10 mins).

STM

TBG samples were prepared using the tear-and-stack method with poly-propylene carbonate (PPC) as a polymer to sequentially pick up h-BN, half of a piece of graphene followed by the second half with a twist angle. This structure was flipped over and placed on an Si/SiO_2 chip with no further processing of the polymer. Direct contact was made with TBG by microsoldering with Field's metal at a temperature of 65 °C under ambient conditions. No further annealing or processing of samples was performed before measurement. Ultrahigh-voltage STM and spectroscopy measurements were carried out in a home-built, ultrahigh-voltage STM at a temperature of 5 K. All tips used in this study were prepared on Au(111) and calibrated spectroscopically before measurement of graphene. Several freshly prepared tips were used in this study to ensure the consistency and accuracy of findings.

Exciton calculation

A phenomenological calculation of exciton Rydberg state hybridization is provided here. We assumed that Ns Rydberg states have energy $E^{(Ns)}(n)$ (Supplementary Fig. 10), dependent on average carrier density n in the TBG layers, where N is the principle quantum number of the Rydberg state. Quasi-particle gap and exciton binding are sensitive to local charge distribution, both indirectly controlled by average carrier density. With the marked variation in charge density distribution in TBG at length scale already comparable to exciton radius in monolayer WSe_2, Rydberg states in the pristine monolayer are no longer eigenstates of Coulomb binding in the presence of doped TBG; hybridization of Rydberg states that are similar in energy then becomes substantial. We considered the coupling of the 2s state with two nearby states (3s and 4s), with matrix elements $t_{23}(n)$ and $t_{34}(n)$ dependent on average carrier density. The energy (E_N) of the hybridized state can be calculated by solving

$$H = \begin{bmatrix} E^{(2s)} & t_{23} & 0 \\ t_{23}^* & E^{(3s)} & t_{34} \\ 0 & t_{34}^* & E^{(4s)} \end{bmatrix}.$$

The spectral function of the hybridized state can then be calculated:

$$A(E,n) = -\frac{1}{\pi} Im \sum_{N=2}^{4} \frac{|c_2|^2}{E - E_N + i\gamma}$$

with c_N being the component of Ns Rydberg state and γ band broadening. The simulated spectrum shown in Fig. 3d was obtained using the carrier density dependence of the parameters given in Supplementary Fig. 10. Further discussion on moiré potential-induced exciton hybridization is given in Supplementary Note 2.

Data availability

Source data are provided with this paper. All other data are available from the corresponding author on reasonable request.

Code availability

Codes used for data analysis in this study are also available from the corresponding author on reasonable request.

References

49. Popert, A. et al. Optical sensing of fractional quantum Hall effect in graphene. *Nano Lett.* **22**, 7363–7369 (2022).

Acknowledgements

We thank J. L. Li and H. Yu for helpful discussions. This work was supported mainly by the US Department of Energy Basic Energy Sciences under award no. DE-SC0018171 (to X.X., M.H. and J.C.). Sample fabrication was partially supported by the ARO MURI programme (grant no. W911NF-18-1-0431 to M.H.). Electrical transport measurement was partially supported by the US National Science Foundation through the UW Molecular Engineering Materials Center, a Materials Research Science and Engineering Center (no. DMR-1719797 to X.X. and M.Y.). STM/spectroscopy measurement is supported by the Center on Programmable Quantum Materials, an Energy Frontier Research Center funded by the US Department of Energy, Office of Science, Basic Energy Sciences, under award no. DE-SC0019443 (to A.P. and E.S.). Work at the University of Hong Kong is supported by the Research Grants Council of Hong Kong SAR (nos. AoE/P-701/20 and HKU SRFS2122-7S05 to W.Y. and H.Z.). W.Y. also acknowledges support by the New Cornerstone Science Foundation. K.W. and T.T. acknowledge support from JSPS KAKENHI (grant nos. 19H05790, 20H00354 and 21H05233). X.X. acknowledges support from the State of Washington-funded Clean Energy Institute and from the Boeing Distinguished Professorship in Physics.

Author contributions

M.H. and J.C. performed transport and optical reflection measurements, under the supervision of X.X. and M.Y. M.H. fabricated samples. M.H., J.C., M.Y., W.Y. and X.X. analysed and interpreted results. H.Z. and W.Y. performed theoretical calculations. E.S. and A.P. performed STM measurements and analysed results. J.Y. synthesized and characterized bulk WSe_2 crystals. T.T. and K.W. synthesized h-BN crystals. M.H., X.X., W.Y., J.C. and H.Z. wrote the paper with input from all authors. All authors discussed the results.

Competing interests

The authors declare no competing interests.

Additional information

Supplementary information The online version contains supplementary material available at https://doi.org/10.1038/s41563-023-01713-y.

Correspondence and requests for materials should be addressed to Wang Yao or Xiaodong Xu.

Peer review information *Nature Materials* thanks Olga Kazakova and the other, anonymous, reviewer(s) for their contribution to the peer review of this work.